Journal of Machine Engineering, 2022, Vol. 22, No. 1, 111–123
ISSN 1895-7595 (Print) ISSN 2391-8071 (Online)

Received*: 06 February 2022* / Accepted: *07 March 2022* / Published online: *10 March 2022*

machining, Ti6Al4V,
machine learning, SPH,
meshfree methods

Hagen KLIPPEL[1*], Eduardo Gonzalez SANCHEZ[1]
Margolis ISABEL[2], Matthias RÖTHLIN[3],
Mohamadreza AFRASIABI[2], Kuffa MICHAL[1],
Konrad WEGENER[1]

CUTTING FORCE PREDICTION OF TI6AL4V USING A MACHINE LEARNING MODEL OF SPH ORTHOGONAL CUTTING PROCESS SIMULATIONS

The prediction of machining processes is a challenging task and usually requires a large experimental basis. These experiments are time-consuming and require manufacturing and testing of different tool geometries at various process conditions to find optimum machining settings. In this paper, a machine learning model of the orthogonal cutting process of Ti6Al4V is proposed to predict the cutting and feed forces for a wide range of process conditions with regards to rake angle, clearance angle, cutting edge radius, feed and cutting speed. The model uses training data generated by virtual experiments, which are conducted using physical based simulations of the orthogonal cutting process with the smoothed particle hydrodynamics (SPH). The ML training set is composed of input parameters, and output process forces from 2500 instances of GPU accelerated SPH simulations. The resulting model provides fast process force predictions and can consider the cutter geometry in comparison to classical analytical approaches.

1. INTRODUCTION

Models for the prediction of process forces from metal cutting operations can be classified into empirical, analytical and numerical approaches. Empirical models like the Kienzle equation [1] are fitted to measured process forces from cutting experiments. Based on experimental observations, analytical modelling approaches were introduced with Ernst [2] and Merchant [3]. These were refined with Oxley's [4] machining theory and extended to more recent material models in [5] and [6]. These approaches excel in very low computational times, but all these models have in common that they lack the consideration of the clearance angle or the influence of the cutting edge radii. The availability of computers enabled the use of numerical approaches and it became possible to simulate the cutting process on a physical

[1] IWF, ETH Zürich, Switzerland
[2] IWF/inspire, ETH Zürich, Switzerland
[3] Federal Office of Meteorology & Climatology, MeteoSwiss, Switzerland
[*] E-mail: hklippel@ethz.ch
https://doi.org/10.36897/jme/147201

level including a detailed representation of the cutter geometry. Critical problems in the numerical modeling approach of the cutting process are the modeling of the material behavior as well as the numerical method to resolve the continuum, see also [7] and [8]. Mostly the finite element method (FEM) is used for numerical cutting simulations. The FEM is a versatile tool, but frequent remeshing is required due to the large deformations, which occur in the simulation of machining processes. The time consuming remeshing can be avoided by using an alternative numerical method, which does not rely on a mesh but particles: smoothed particle hydrodynamics (SPH). Particles move with the continuum and can easily handle large deformations. The SPH is well suited for massive parallelization on the GPU which results in short runtimes of machining simulations, see for example [9].

In the present study, the SPH is used to perform virtual experiments, where instead of real cutting experiments, numerical simulations of orthogonal cuts are performed based on a design of experiments (DOE). The results of the virtual experiments are used to train a machine learning (ML) model, which can then be used to predict process forces for different tool geometries (clearance angles, rake angles, and cutting edge radii) at different process conditions. Theoretical aspects of the SPH and ML- theory are introduced hereafter. This is followed by a description of the numerical model used to generate the virtual experiments and an explanation of the ML model. Finally, the ML model is used to predict cutting and feed forces for different clearance angles, rake angles, and cutting edge radii at varying feed and cutting speeds. The predictions are compared to experimental results from the literature.

2. THEORETICAL BACKGROUND

This chapter is devoted to shortly outlining the fundamentals of the SPH used for the virtual experiments and is followed by a brief introduction to machine learning.

2.1. SPH FUNDAMENTALS

The SPH was introduced 1977 in astrophysics by Gingold and Monaghan [10] for the calculation of a smoothed density from point clouds. A simple derivation of the method is based on the partition of unity [11], where a field value at a spatial location x can be determined as:

$$f(x) = \int_{\mathbb{R}^d} \delta(x - x') f(x') d\Omega_{x'} \;\; \forall x \epsilon \mathbb{R}^d \tag{1}$$

The Dirac-delta function $\delta(x)$ in equation (1) has two important properties:

$$\int_{-\infty}^{+\infty} \delta(x) dx = 1 \tag{2}$$

$$\int_{-\infty}^{+\infty} \delta(\zeta - x) f(\zeta) d\zeta = f(x) \tag{3}$$

Replacing the Dirac-delta function $\delta(x)$ with a smoothing function, the so-called Kernel $W(x-x',h)$; e.g., the Gauß-function, with h being a smoothing length, the behavior of the -NEWDirac-delta can be reproduced for the limit:

$$\lim_{h\to 0} W(x-x',h) = \delta(x-x') \tag{4}$$

Inserting (4) into equation (3) gives an approximation of the function value $f(x)$ at x:

$$< f(x) >= \int_{-\infty}^{+\infty} W(x-x',h) f(x') dx' \tag{5}$$

This can be integrated within a discrete neighborhood using a Riemann-sum:

$$< f_i >= \sum_j f_j \, W\big(x_{ij},h\big)\Delta V_j \tag{6}$$

with the point index i at which the function value is to be approximated by its neighbor points j, x_{ij} is the spatial distance between point i and j and ΔV_j being an integration weight of point j. Computation of the function's derivative leads to

$$< \nabla f_i >= \sum_j f_j \, \nabla W\big(x_{ij},h\big)\Delta V_j \tag{7}$$

where only the derivative of the Kernel $W\big(x_{ij},h\big)$ is required. In this way, derivatives of values given at point cloud locations can be computed without the requirement of a functional description or a mesh-based relation between these points (particles). With this meshfree approximation, derivatives in the continuum mechanics equation can be computed by sums of discrete values in the neighborhood of the particles. Meshfree techniques were adopted in the early 1990s to structural simulations [12] and for numerical cutting simulations first in [13]. At the institute of machine tools and machine tools (IWF) of ETH Zürich, the software *mfree_iwf* was developed in the past years for SPH-based machining simulations [14]. The software is capable of performing CPU as well as GPU-enhanced computations of metal cutting simulations. It establishes the state-of-the-art in SPH simulations as it facilitates the most recent correctors and stabilization measures for mechanical [15] and thermal simulations [16]. The software successfully demonstrated computationally highly efficient metal cutting simulations [9], identification of friction parameters [17], and its ability to adaptive refinements [18]. Further, single grain grinding simulations of engineered grinding tools [19] were successfully demonstrated. In the presented investigation, the software is used to simulate orthogonal cuts with a flow stress model according to Johnson and Cook [20]. The model is commonly used to describe metal plasticity within machining simulations and is given as:

$$\sigma_Y = \left(A + B\cdot \varepsilon_{pl}^{n}\right)\cdot\left(1 + C\cdot ln\frac{\dot{\varepsilon}_{pl}}{\dot{\varepsilon}_{pl}^{0}}\right)\cdot\left(1-\frac{T-T_{ref}}{T_f-T_{ref}}\right)^{m} \tag{8}$$

With A, B, C, m and n being material parameters, ε_{pl} the current plastic strain, $\dot{\varepsilon}_{pl}$ the current plastic strain rate and T the current temperature. T_f is the melting temperature, T_{ref} is the

reference temperature and $\dot{\varepsilon}_{pl}^{0}$ the reference plastic strain rate. The first two terms describe hardening due to plastic strain and plastic strain rate, respectively. The third term controls thermal softening upon increasing temperature. In this investigation, material parameters for Ti6Al4V according to [21] are used.

2.2. MACHINE LEARNING

Machine learning is a set of algorithms capable of independently learning patterns within a dataset. Due to the progress in parallel computing technologies, machine learning is causing a paradigm shift in many areas of science and engineering [22, 23]. A specific subset of machine learning is deep learning, which contains algorithms based on neural networks capable of learning structures and patterns from large amounts of data. Because deep learning algorithms are very good at discovering intricate structures in high-dimensional data, it is well applicable to many domains. Inspired by the human brain, neural networks are the core of deep learning. In its most basic and general form, the multi-layer perceptron (MLP) is composed of an input layer, hidden layers, and an output layer. Every layer consists of activation units (sometimes labeled neurons), which are connected with the units from previous layers through weighted edges. In supervised learning, the training data that is fed to the algorithm already includes the desired solution, called labels. During the training of the neural network, the weights are adapted such that the output of the neural network for each training sample approaches the desired solution. It is important that there is enough data for training to reasonably capture the relationship that may exist between the input features and the labels. One of the advantages of machine learning is its computation time. Cambioni et al. [24] show that their machine learning model, which is trained using SPH simulations for giant impacts, is able to accurately map the parameter space to the outcome of the simulations and runs in less than a second compared to days of simulation efforts. Specifically, once the ML model is trained on the available data, the model parameters can be saved, thus allowing for very fast inference. The usage of ML models for fast interpolation from simulation data is an emerging area of research [25–28].

3. NUMERICAL MODEL FOR VIRTUAL EXPERIMENTS

A parameterized numerical model is created for the orthogonal cutting simulation of Ti6Al4V. The geometry of the numerical model is depicted in Fig. 1. The cutter is modeled as a rigid body with an analytical description of the cutter geometry comprising the clearance angle α, rake angle γ, and the cutting edge radius r_n. The workpiece is discretized with particles, where the model height w and the model length l are related to the feed f (uncut chip thickness) by $w = 3f$ and $l = 10f$, respectively. Along height and length direction 30×100 particles are used giving a total number of particles of 3000. Plastic dissipation into

heat is considered with a Taylor-Quinney coefficient of η = 0.9, and the heat conduction is considered in the workpiece only. Friction between tool and workpiece is modeled with a Coulomb model and a constant friction coefficient of μ = 0.35 [29] without consideration of frictional heating.

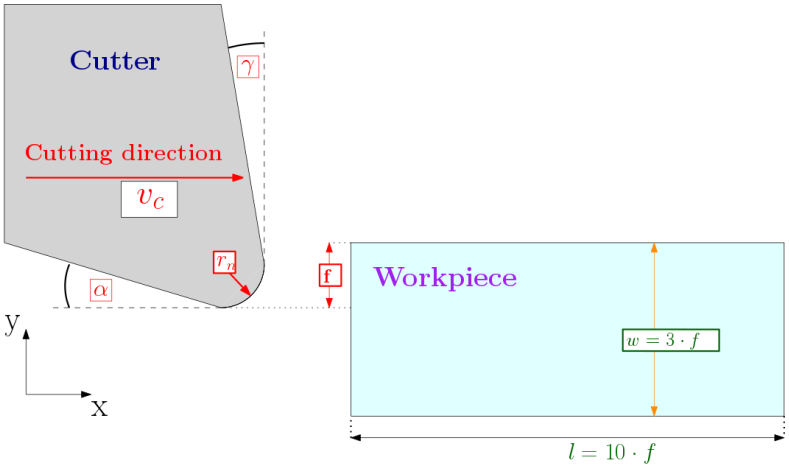

Fig. 1. Geometry of the numerical model of the orthogonal cut

The material properties used in the numerical simulations are provided in Table 1. The constitutive parameters for the Johnson-Cook flow stress model stem from an inverse parameter identification conducted in [21] based on a cutting experiment with a cutting speed of $v_c = 381$ m/min and a feed of $f = 0.1$ mm. An uncoated cutter has been used in this experiment and the cutter geometry was measured with the following parameters: rake angle γ = 0°, clearance angle α = 7° and a cutting edge radius r_n = 33 µm. The material batch of Ti6Al4V in [21] has a proof strength of $R_{p0,2\%} = 869$ MPa and a tensile strength of $R_m = 952$ MPa.

Table 1. Material properties of Ti6Al4V used in the virtual experiments

Parameter	Symbol	Value	Unit	Data Source
Young's modulus	E	110	GPa	[30]
Poisson ratio	ν	0.35	-	[30]
Density	ρ	4430	kg/m³	[30]
Specific heat	c_p	526	J/kgK	[30]
Thermal conductivity	λ	6.8	W/mK	[30]
Friction coefficient	μ	0.35	-	[29]
Taylor-Quinney coefficient	η	90%	-	[31]
JC constant	A	852.1	MPa	[21]
JC constant	B	338.9	MPa	[21]
JC constant	C	0.02754	-	[21]
JC constant	m	0.5961	-	[21]
JC constant	n	0.148	-	[21]
JC constant	$\dot{\varepsilon}_{pl}^{0}$	1.0	1/s	[21]
Reference temperature	T_{ref}	300	K	
Melting temperature	T_f	1836	K	

A full factorial design is chosen to perform 2’500 virtual experiments in total as input for the machine learning model. The corresponding parameter ranges of the DOE are given in Table 2. The simulations are computed on 5 GPUs (NVidia GTX660, GTX970, GTX1650, Tesla P100, and Quadro GP100) within five days. The process force results from the SPH simulations are standardized to a cutting width of b = 1 mm and all results of the DOE are displayed in the charts in Fig. 2 versus all input and output quantities. An increasing rake angle γ leads to decreasing process forces while the cutting edge radius r_n has almost no impact on the cutting force but a moderate impact on the feed force. The feed f has a major impact on the cutting force, while the feed force shows larger scattering towards increasing feeds.

Table 2. DOE parameter ranges

Quantity	Symbol	Unit	Steps	Values
Clearance angle	α	°	5	5, 10, 15, 20, 25
Rake angle	γ	°	5	-10, 0, 10, 20, 30
Cutting edge radius	r_n	µm	5	10, 20, 30, 40, 50
Feed (uncut chip thickness)	f	mm	4	0.05, 0.1, 0.2, 0.3
Cutting speed	v_c	m/min	5	20, 100, 200, 350, 500

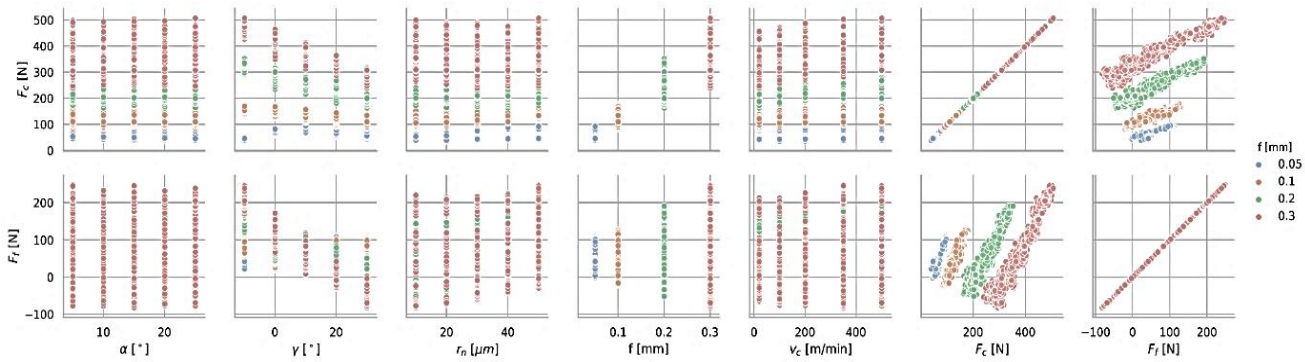

Fig. 2. SPH results from the DOE. The color of the data points corresponds to the feed of the respective simulation

4. MACHINE LEARNING MODEL

A total of 2’500 simulations, with the parameters given in Table 2, are used to train an ML model to interpolate the simulation results over a continuous range of input parameters. can replace the classical simulations for faster inference. The trained model MLPs are universal approximators and can therefore be used as suggested by [32] to approximate the SPH simulations. The simulations can be represented as a function S: $\mathbb{R}^5 \rightarrow \mathbb{R}^2$. The input is a vector $[\alpha, \gamma, r_n, f, v_c]$, where $\alpha, \gamma, r_n, f, v_c$ are the controllable parameters of the experiment. $[F_c, F_f]$ is the output vector, where F_c, F_f are the cutting force and the feed force measured in the virtual experiment. For better performance, two separate MLPs are trained for both forces. Each MLP consists of five input units and a single output unit for the respective force. Fig. 3 shows the architecture of the MLP.

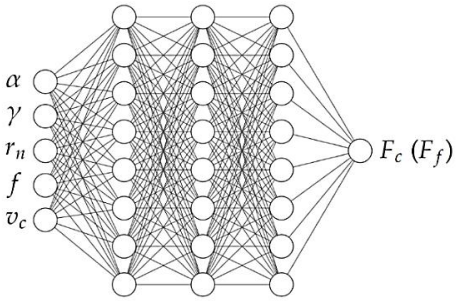

Fig. 3. Representation of the two MLPs used to approximate the simulations. The MLPs have three hidden layers. For readability reasons the layers in the image have only 8 units, while in the implemented models they have a size of 32

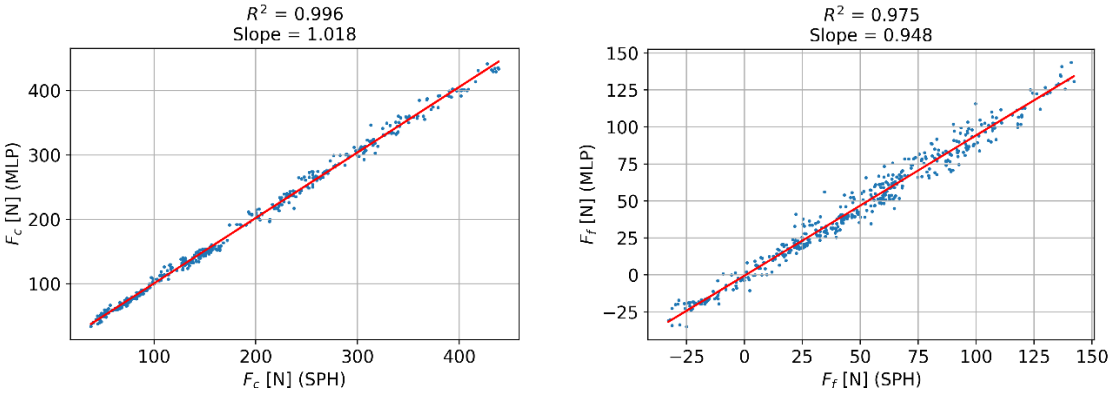

Fig. 4. Representation of the performance of the model on the unseen validation test. The model successfully predicts the values of the forces generated by the simulation with reasonable accuracy

The MLPs have been implemented with the framework Keras + Tensorflow 2.0. This framework provides an optimized environment to train MLPs using backpropagation on different versions of the gradient descent algorithm. The hyper-parameters used for the training are sigmoid activation functions in all the hidden layers units, Adam optimizer for the gradient descent implementation, mean squared error (MSE) as the loss function, a batch size of 16, and 50 epochs for each MLP. The data has been scaled before the training, so the input features of the MLPs have mean zero and unit variance. These values probably came from divergences due to numerical instabilities in the simulation.

With these steps, the models acquire a predictive power of $R^2_{F_c} = 0.996$ in the validation set for F_c and $R^2_{F_f} = 0.948$ for F_f.

4.1. ADVANTAGES AND DISADVANTAGES OF USING AN ML INTERPOLATOR

Training an ML model on data solely from SPH simulations has uncovered several advantages and disadvantages. The advantages are listed in the following points:

- ML models provide a fast and efficient interpolation method to new values within the parameter ranges of the training sample with the computational effort being a fraction of a second. This is helpful to identify trends without the need to run costly simulations.

- Because ML models look for generalizations in all the given data, they may be more robust and accurate compared to the simulations. SPH and similar particle simulation methods are numerically unstable, and some conditions may cause divergences in the results. The ML model may identify these divergences as outliers, which can result in more accurate edictions.

On the other hand, the ML model also presents some disadvantages:

- Although the ML model can help identify simulation errors by generalizing over the entire dataset, this attribute may also cause disadvantages. Certain parameter combinations may cause divergences in the process outputs, which are explainable from a physical standpoint instead of being simulation errors. Hence, the ML model may not be able to distinguish between correct physical divergences and simulation errors.
- ML algorithms depend on their underlying structure and the chosen hyperparameters. Thus, given a different algorithm or different choices of hyperparameters, the resulting function explaining the relationship between the input parameters and the process outputs may differ.

Figure 5. shows the relationship between the cutting forces and the feed forces of both the simulations (markers) and the ML predictions (lines). Because the ML model allows for interpolation, intermediary results are easily available for the ML model, which for the SPH simulations would require additional simulation time. Thus, the ML model reveals relationships between the process forces, the feed force, and the cutting edge radius, which may not be visible by the SPH simulations alone.

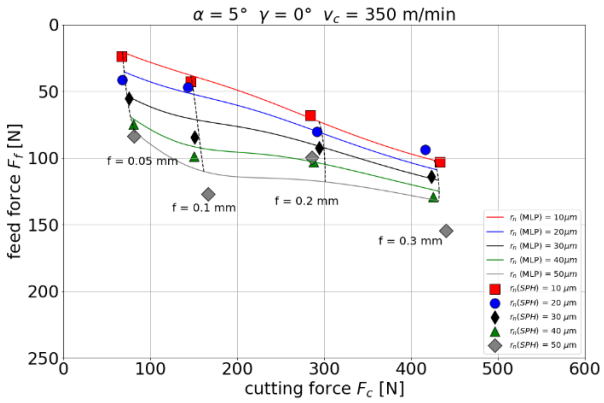

Fig. 5. Influence of the cutting edge radius r_n and feed f on cutting forces F_c and feed forces F_f, standardised to a cutting width of b = 1mm at v_c = 350 m/min with a clearance angle of α = 5° and a rake angle of γ = 0°. Results from the SPH simulation and the interpolation with the ML model

5. ML MODEL PREDICTIONS

The fitted ML model from chapter 0 is used to calculate the process forces for varying cutting edge radii r_n, clearance angles α, rake angles γ, feed f and cutting speeds v_c. The results are compared against experimental results on Ti6Al4V from Wyen [29], who investigated the effect of varying cutting edge radii as well as different rake and clearance angles on the process forces with uncoated tools. In his experiments each test was performed

with a fresh cutter insert to exclude any geometrical changes due to wear effects. The material batch of Ti6Al4V in the experiments of Wyen [29] has a proof strength of $R_{p0,2\%} = 920$ MPa and a tensile strength of $R_m = 965$ MPa, which indicates a higher strength than the batch of [21].

5.1. INFLUENCE OF THE CUTTING EDGE RADIUS ON SPECIFIC CUTTING AND FEED FORCES

The specific cutting and feed forces are predicted for varying cutting edge radii in the range of $r_n = 10 \ldots 50\,\mu m$, varying feeds from $f = 0.01 \ldots 0.2\,mm$ and for constant cutting speed $v_c = 70\,m/min$, clearance angle $\alpha = 8°$ and rake angle $\gamma = 10°$. In Fig. 6 trends for both, specific cutting and feed force, are captured well. The magnitude of the specific cutting force is overpredicted by 10~20% at low feeds while for high feeds it is slightly underpredicted. It has to be noted, that the ML model is extrapolating towards low feeds since the minimum feed in the virtual experiments was f_{min} = 0.05, see also Table 2. The magnitude of the specific feed force is underestimated throughout the complete feed range, but qualitatively correctly predicts lower specific feed forces for decreasing cutting edge radii.

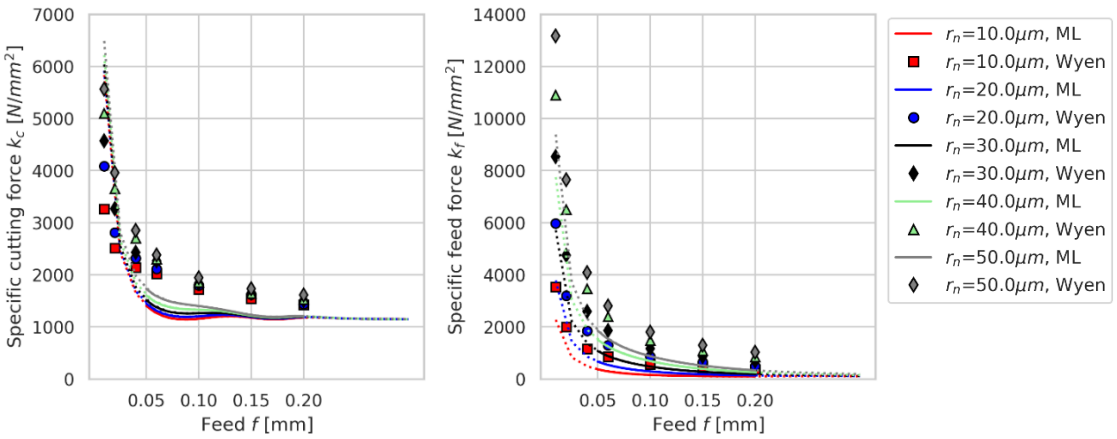

Fig. 6. Influence of the cutting edge radius r_n and feed f on specific cutting and feed forces k_c and k_f, at v_c=70m/min with a clearance angle of α=8° and a rake angle of γ=10°. Experimental results from [29] are shown at discrete points, ML-model predictions are shown with lines where dotted lines are in the extrapolation range of the ML model

5.2. INFLUENCE OF THE CUTTING EDGE RADIUS ON THE PROCESS FORCES

In a second example, the influence of the cutting edge radius r_n on the process forces is investigated. For this purpose, the cutting edge radius is varied from r_n = 10…50 µm and the feed from f = 0.01…0.3 mm. The other process parameters are set constant to a cut speed of v_c = 70 m/min, the clearance angle to α = 8° and the rake angle to γ = 10°. In Fig. the cutting forces predicted with the ML model show a similar trend but with about 10…20% smaller magnitude than observed in the experiments from Wyen [29]. The influence of the cutting edge radii on the cutting force is smaller in the ML prediction and decreases even further towards higher feeds which is in contrast to the experimental observation. The ML model

predicts too low feed forces for all feeds and all cutting edge radii. Furthermore, at this rake angle, the feed forces from the ML model decrease with increasing feed which is opposed to the experimental observation.

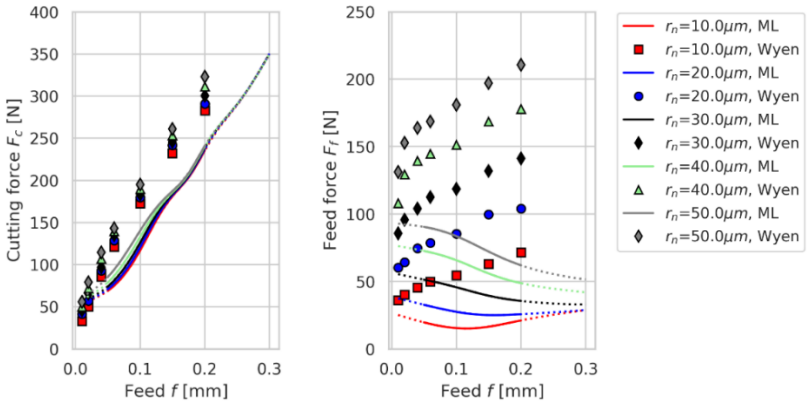

Fig. 7. Influence of the cutting edge radius r_n and feed f on cutting forces F_c and feed forces F_f, standardised to a cutting width of b = 1 mm at v_c = 70 m/min with a clearance angle of α = 8° and a rake angle of γ = 10°. Dots are experimental results from [29] and lines are predicted with the ML model where dotted lines show extrapolated results of the ML model

5.3. INFLUENCE OF THE RAKE ANGLE ON THE PROCESS FORCES

In this part of the investigation, the process forces are computed for different rake angles with varying feeds. The results are shown in Fig. 8 together with experimental values from Wyen [29]. The predicted cutting forces are 20% higher in the low feed range while they are 20% smaller at higher feeds. The cutting force dependency on the rake angle is covered well, where the lowest rake angle (γ = 0°) results in the highest cutting force, which is similar to the experimental observation. The feed force is underpredicted over the whole feed range. It is observed that towards higher rake angle γ, the feed force prediction worsens, and at γ = 15°, the trend with increasing feed is even opposite to the experimental observation.

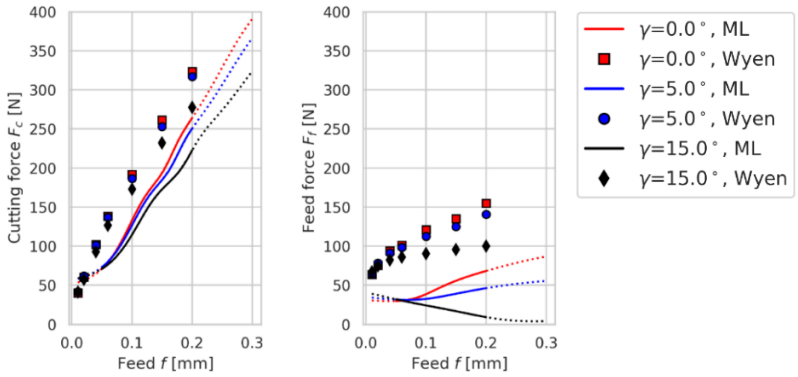

Fig. 8. Influence of different rake angles γ and feed f on cutting forces F_c and feed forces F_f, standardized to a cutting width of b = 1 mm at v_c = 70 m/min with a clearance angle of α = 10° and a cutting edge radii of r_n = 20±1µm. Dots show experimental results from Wyen [29] and lines are results predicted with the ML model, where dotted lines show extrapolation results of the ML model

6. SUMMARY and CONCLUSION

A process force prediction tool for orthogonal cutting of Ti6Al4V was proposed based on a machine learning model. The novelty in this approach is that cutting experiments are not required. Instead, virtual experiments are conducted by utilization of a numerical model of the orthogonal cutting process of Ti6Al4V. The proposed methodology avoids time consuming cutting experiments with different cutter geometries and process conditions. The machine learning model is trained to 2'500 virtual experiments and subsequently used to predict process forces for various process conditions and cutter geometries. The results are compared to experiments where it was found that the trends of the specific cut and feed force are captured well over a range of different feeds, but with smaller magnitudes than experimentally observed. The cutting edge radii influence on the process forces was qualitatively correctly approximated by the ML model where the process forces increase over increasing cutting edge radii. It was found that the rake angle dependency of the cutting forces can be covered well, but for the feed force component, a correct trend is predicted only for the smallest rake angle while the trend becomes even opposed to experimental observations in Wyen [29] for increasing rake angles. However, such behavior at higher rake angles is known from experiments conducted by Albrecht [33], but in the SPH simulations it occurs already earlier at lower rake angles. The reasons for the deviations are manifold and the main points, based on the author's opinion, are summarized in the following. The JC material parameters which were used for the virtual experiments are derived within a parameter identification procedure from a different material batch of Ti6Al4V with different treatment prior to the cutting than the one used in the experiments by Wyen [29]. This difference in both material batches are reflected in the higher strength values of the material batch of Wyen. It was recognized that feed forces are always underpredicted and towards higher rake angles γ the errors in the ML model prediction increase in comparison to the experiment. On the virtual experiments side this indicates that the underlying numerical simulation model of the orthogonal cutting cannot correctly cover the physics when the rake angle increases. The reason for this is likely due to the constitutive model (Johnson-Cook) and the Coulomb friction law in the numerical simulations. The quality of the numerical predictions is expected to improve under consideration of more physical material models, which for example include effects of the dislocation density and globularization, see [34, 35], or models which incorporate the effect of phase transformations towards higher temperatures [36]. On the other hand, more sophisticated friction models, e.g. with temperature dependent friction coefficients [17] and [37], potentially improve the modelling of the tool-workpiece interaction.

With the proposed improvements to the modeling approach, it is expected that the SPH simulations can be extended to predict also the effect of built-up edges and tool wear on the process forces. On the ML model side, reasons for inaccuracies can arise due to smoothing of the experimental data and extrapolation beyond the experimental data which is seen for example at very low feeds. Further investigations are required in how far the number of evaluations for the DOE can be reduced or optimized, for example by using a fractional factorial plan instead of a full factorial plan, which was used here.

ACKNOWLEDGEMENTS

The authors hereby would like to thank the SNF for partial funding of this work from the project "GPU-Enhanced Metal Cutting Simulation Using Advanced Meshfree Methods" under the grant #200021_149436.

REFERENCES

[1] KIENZLE O., 1952, *Die Bestimmung von Kräften und Leistungen an spanenden Werkzeugen und Werkzeugmaschinen*, VDI-Z, 94, 299–305.
[2] ERNST H., 1938, *Physics of Metal Cutting*, Cincinnati Milling Machine Company.
[3] MERCHANT M.E, 1945, *Mechanics of the Metal Cutting Process. II. Plasticity Conditions in Orthogonal Cutting*, Journal of applied physics, 16/6, 318–324.
[4] OXLEY P.L.B., 1989, *The Mechanics of Machining: An Analytical Approach to Assesing Machinability*, Ellis Horwood.
[5] ADIBI-SEDEH A.H., MADHAVAN V., BAHR B., 2003, *Extension of Oxley's Analysis of Machining to Use Different Material Models*, J. Manuf. Sci. Eng. 125/4, 656–666.
[6] LALWANI D.I.; MEHTA N.K., JAIN P.K., 2009, *Extension of Oxley's Predictive Machining Theory for Johnson and Cook Flow Stress Model*, Journal of Materials Processing Technology, 209/12–13, 5305–5312.
[7] ARRAZOLA P.J, ÖZEL T., UMBRELLO D., DAVIES M., JAWAHIR I.S., 2013, *Recent Advances in Modelling of Metal Machining Processes*, Cirp Annals, 62/2, 695–718.
[8] SRIDHAR P., PRIETO J.M.R., DE PAYREBRUNE K.M., 2020, *Discretization Approaches to Model Orthogonal Cutting with Lagrangian, Arbitrary Lagrangian Eulerian, Particle Finite Element Method and Smooth Particle Hydrodynamics Formulations*, Procedia CIRP, 93, 1496–1501.
[9] RÖTHLIN M., KLIPPEL H., AFRASIABI M., WEGENER K., 2019, *Metal Cutting Simulations Using Smoothed Particle Hydrodynamics on the GPU*, The International Journal of Advanced Manufacturing Technology, 102/ 9–12, 3445–3457.
[10] GINGOLD R.A., MONAGHAN J.J., 1977, *Smoothed Particle Hydrodynamics: Theory and Application to Non-Spherical Stars*, Monthly Notices of The Royal Astronomical Society, 181/3, 375–389.
[11] LI S., LIU W.K., 2004, *Meshfree Particle Methods*, Springer, Berlin.
[12] LIBERSKY L.D., PETSCHEK A.G., 1991, *Smooth Particle Hydrodynamics with Strength of Materials*, Soccoro New Mexico, 87801.
[13] HEINSTEIN M., SEGALMAN D., 1997, *Simulation of Orthogonal Cutting with Smooth Particle*, Sandia National Laboratories.
[14] RÖTHLIN M., 2019, *Meshless Software Tool to Simulate Metal Cutting Operations by Employing Contemporary Numerical Methods*, Dissertation, ETH Zürich.
[15] RÖTHLIN M., KLIPPEL H., WEGENER K., 2018, *Meshless Methods for Large Deformation Elastodynamics*, arXiv preprint arXiv:1807.01117.
[16] AFRASIABI M., RÖTHLIN M., WEGENER K., 2019, *Contemporary Meshfree Methods for Three Dimensional Heat Conduction Problems*, Archives of Computational Methods in Engineering, 1–35.
[17] AFRASIABI M., MEIER L., RÖTHLIN M., KLIPPEL H., WEGENER K., 2020, *GPU-Accelerated Meshfree Simulations for Parameter Identification of a Friction Model in Metal Machining*, International Journal of Mechanical Sciences, 105571.
[18] AFRASIABI M., RÖTHLIN M., KLIPPEL H., WEGENER K., 2019, *Meshfree Simulation of Metal Cutting: an Updated Lagrangian Approach with Dynamic Refinement*, International Journal of Mechanical Sciences, 160, 451–466.
[19] RÖTHLIN M., KLIPPEL H., AFRASIABI M., WEGENER K., 2019, *Meshless Single Grain Cutting Simulations on the GPU*, International Journal of Mechatronics and Manufacturing Systems, 12/3–4, 272–297.
[20] JOHNSON G.R., COOK W.H., 1983, *A Constitutive Model and Data for Metals Subjected to Large Strains, High Strain Rates and High Temperatures*, Proceedings of the 7th International Symposium on Ballistics, 21/1.
[21] KLIPPEL H., 2021, *Constitutive Equations for Simulation of Metal Cutting with Meshless Methods on GPU*, Dissertation, ETH Zürich.
[22] JUMPER J., EVANS R., PRITZEL A., GREEN T., FIGURNOV M., RONNEBERGER O., TUNYASUVUNAKOOL K., BATES R., ŽÍDEK A., POTAPENKO A., BRIDGLAND A., 2021. *Highly Accurate Protein Structure Prediction with AlphaFold*, Nature, 596, 583–589.
[23] CARLEO G., CIRAC I., CRANMER K., DAUDET L., SCHULD M., TISHBY N., VOGT-MARANTO L. ZDEBOROVÁ L., 2019, *Machine Learning and the Physical Sciences. Reviews of Modern Physics*, 91/4, 045002.
[24] CAMBIONI S., 2019, *Realistic On-the-fly Outcomes of Planetary Collisions: Machine Learning Applied to Simulations of Giant Impacts*, The Astrophysical Journal, 875/1, 40, https://doi.org/10.48550/arXiv.1903.04507.
[25] JAKOB J., GROSS M., GÜNTHER T., 2020, *A Fluid Flow Data Set for Machine Learning and its Application to Neural Flow Map Interpolation*, IEEE Transactions on Visualization and Computer Graphics, 27/2, 1279–1289.
[26] LANGER M.F., GOESSMANN A., RUPP M., 2020, *Representations of Molecules and Materials for Interpolation of Quantum-Mechanical Simulations via Machine Learning*, arXiv preprint arXiv:2003.12081.

[27] WOODWARD M., TIAN Y., HYETT C., FRYER C., LIVESCU D., STEPANOV M., CHERTKOV M., 2021, *Physics Informed Machine Learning of SPH: Machine Learning Lagrangian Turbulence*, arXiv Preprint arXiv:2110.13311.
[28] SHI C., WANG Y., 2021, *Non-Parametric Machine Learning Methods for Interpolation of Spatially Varying Non-Stationary and Non-Gaussian Geotechnical Properties*, Geoscience Frontiers, 121, .339–350.
[29] WYEN C.F., 2011, *Rounded Cutting Edges and Their Influence In Machining Titanium*, Dissertation, ETH Zürich.
[30] RÜTTIMANN, 2012, *Simulation of Metal Cutting Processes Using Meshfree Methods*, Dissertation, ETH Zürich.
[31] DUCOBU F., ARRAZOLA P.J., RIVIÈRE-LORPHÈVRE E., FILIPPI E., 2021, *On the Selection of an Empirical Material Constitutive Model for the Finite Element Modelling of Ti6Al4V Orthogonal Cutting, Including the Segmented Chip Formation*, International Journal of Material Forming, 3.
[32] CYBENKO G., 1989, *Approximation by Superpositions of a Sigmoidal Function*, Math. Control Signal Systems, 2, 303–314.
[33] ALBRECHT P., 1960, *New Developments in the Theory of the Metal-Cutting Process: Part I. The Ploughing Process in Metal Cutting*, Journal of Engineering for Industry, 82/4, 348–357.
[34] BABU B., LINDGREN L.E., 2013, *Dislocation Density Based Model for Plastic Deformation and Globularization of Ti-6Al-4V*, International Journal of Plasticity, 50, 94–108.
[35] RODRIGUEZ J.M., LARSSON S., CARBONELL J.M., JONSÉN P., 2020, *Dislocation Density Based Flow Stress Model Applied to the PFEM Simulation of Orthogonal Cutting Processes of Ti-6Al-4V*, Materials, 13/8, 1979, https://doi.org/10.3390/ma13081979.
[36] PAN Z., LIANG S.Y., GARMESTANI H., SHIH D.S., 2016, *Prediction of Machining-Induced Phase Transformation and Grain Growth of Ti-6Al-4 V Alloy*, The International Journal of Advanced Manufacturing Technology, 87/1, 859–866.
[37] MOUFKI A., MOLINARI A., DUDZINSKI D., 1998, *Modelling of Orthogonal Cutting with a Temperature Dependent Friction Law*, Journal of the Mechanics and Physics of Solids, 46/10, 2103–2138.